Nanotechnology

PAPER

Differentiation of metallic and dielectric nanoparticles in solution by single-nanoparticle collision events at the nanoelectrode

To cite this article: Popular Pandey *et al* 2020 *Nanotechnology* **31** 015503

View the article online for updates and enhancements.

IOP ebooks™

Bringing you innovative digital publishing with leading voices to create your essential collection of books in STEM research.

Start exploring the collection - download the first chapter of every title for free.

This content was downloaded from IP address 155.41.63.92 on 22/11/2019 at 15:48

IOP Publishing Nanotechnology
Nanotechnology 31 (2020) 015503 (9pp) https://doi.org/10.1088/1361-6528/ab4445

Differentiation of metallic and dielectric nanoparticles in solution by single-nanoparticle collision events at the nanoelectrode

Popular Pandey[1], Javier Garcia[1], Jing Guo[1], Xuewen Wang[1], Dan Yang[2] and Jin He[1]

[1] Physics Department, biomolecular Science Institute, Florida International University, Miami, 33199, United States of America
[2] Advanced Institute of Materials Science, Changchun University of Technology, Changchun 130012, People's Republic of China

E-mail: jinhe@fiu.edu

Received 16 May 2019, revised 15 August 2019
Accepted for publication 13 September 2019
Published 8 October 2019

Abstract

In this work, we demonstrate a highly effective method to generate and detect single-nanoparticle (NP) collision events on a nanoelectrode in aqueous solutions. The nanoelectrode of a nanopore–nanoelectrode nanopipette is first employed to accumulate NPs in solution by dielectrophoresis (DEP). Instead of using amperometric methods, the continuous individual NP collision events on the nanoelectrode are sensitively detected by monitoring the open-circuit potential changes of the nanoelectrode. Metallic gold NPs (GNPs) and insulating polystyrene (PS) NPs with various sizes are used as the model NPs. Due to the higher conductivity and polarizability of GNPs, the collision motion of a GNP is different from that of a PS NP. The difference is distinct in the shape of the transient potential change and its first time derivative detected by the nanoelectrode. Therefore, the collision events by metallic and insulating NPs on a nanoelectrode can be differentiated based on their polarizability. DEP induced NP separation and cluster formation can also be probed in detail in the concentrated mixture of PS NPs and GNPs.

Supplementary material for this article is available online

Keywords: nanopore, nanoelectrode, nanopipette, single-entity, nanoparticle collision, potential sensing

(Some figures may appear in colour only in the online journal)

1. Introduction

Nanoparticles (NPs) have been widely used in biomedical, energy and environmental applications [1–3]. Due to the ubiquitous nature of the synthetic and biological NPs around us, it is very important to have reliable, cost effective and facile methods to study different properties of the NPs. Single-entity electrochemistry techniques have been developed rapidly in NP analysis, providing new insights different from the traditional ensemble measurements [4, 5]. In the last two decades, the nanopore based techniques have been developed into a powerful method to study NPs at single-NP level [6–9]. Utilising the ionic current change induced by the single-NP translocation event, the shape, charge and even dynamic orientation of NP can be revealed [10–17]. Another technique, the electrochemical detection of single-NP collisions on an ultra-small electrode (UME, micron- and nanoscale) has also emerged as a very useful electrochemical method to

 © 2019 IOP Publishing Ltd Printed in the UK

study individual NPs in solution [18–21]. The so called nanoparticle nano-impact technique enable us to characterise, quantify and detect the nanoparticles and biological entities [22]. Also, they allow us to understand the inter-particle interactions and the aggregation of NPs in the solution and at the UME surface; probe the redox reaction kinetics of catalytic NPs and of electroactive species at the surface of NPs; and obtain information on the surface chemistry of NPs [23–26].

To date, most single-NP collision experiments are measured by amperometric methods. Typically, redox active molecules and/or catalytically active NPs are needed [27–36] in order to amplify the electrochemical current to at least pA level for detection. Instead of current sensing, it has been demonstrated that the NP collision events can also be detected by the open-circuit potential change at the UME [37]. The potential change induced by the NP collision events is typically big enough for the potentiometric method and no extra signal amplification method is needed. Therefore, it is simpler and suitable for many biological applications. In addition, the noise of potentiometric method is smaller at the same bandwidth, allowing for higher sensitivity and faster detection. Although all of these advantages, the potentiometric method is still rarely used in single-entity studies and thus worth to be further explored.

We are motivated to integrate two promising single-entity electrochemistry techniques, the nanopore technique and the potentiometric based nano-impact technique, together to study NPs simultaneously. The quartz nanopipette can be an extremely versatile platform to integrate both methods. We have shown that a nanopore-carbon nanoelectrode (CNE) nanopipette can detect both the ionic current and open-circuit potential changes induced by the transport and translocation of individual gold NPs (GNPs) or polystyrene NPs (PS NPs) when they approach and pass through the nanopore [38, 39]. However, NP collision events at the CNE are rarely observed in previous studies, thus have not been investigated by using the new approach by nanopore–nanoelectrode nanopipette. To enable the nanopore–nanoelectrode nanopipette based multifunctional NP detection, it is important to develop new approaches to generate and detect NP-CNE collision events using the CNE of the nanopipette.

In this report, we demonstrate that continuous NP-CNE collision events can also be generated under the proper condition. Previously, we have demonstrated that the alternating current dielectrophors (AC DEP) can be applied to effectively accumulate the NP near the nanopore and enhance throughput for the NP translocation measurement [38]. Here, the NPs are steered preferentially towards the CNE side. After trapping, a large fraction of pre-concentrated NPs collides at the CNE, instead of translocating through the nanopore. Thus, the NP-CNE collision signals dominate the observed signal. Based on the recorded potential signal, the motion pattern of GNP is different from PS NP in the collision events at the CNE. Such difference is distinct in the potential change signal, which can be used to separate the GNPs from the PS NPs in real-time even in a concentrated NP mixture.

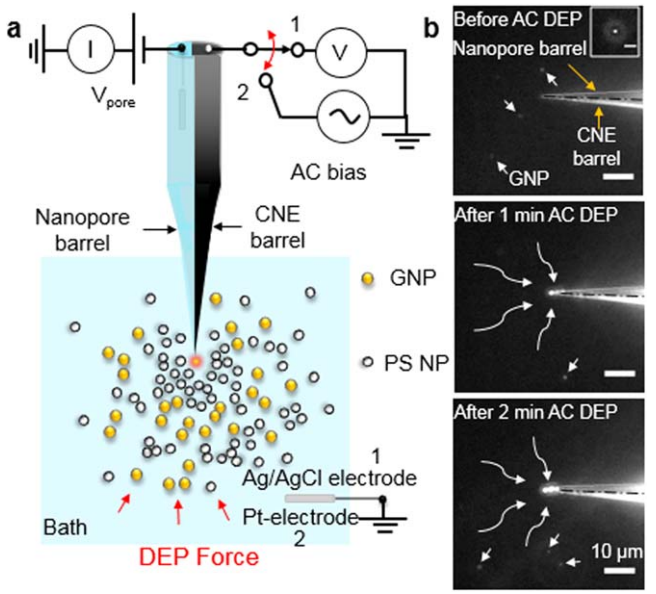

Figure 1. (a) The schematic of the experimental setup (not to scale). V_{pore} is the applied bias. The AC bias source and Pt-electrode are for AC DEP trapping purpose. (b) DFM images of GNPs accumulation near the nanopipette apex by AC DEP. The black dash lines represent the middle separation between two barrels. The bright dots indicated by white arrows are GNPs. The zoom-in of one dot is shown in the inset (the scale bar is 4 μm). The curved white arrows indicate the motion of GNPs towards the nanopipette apex.

2. Experimental methods

2.1. Materials and reagents

ACS grade chemicals (e.g. Phosphate Buffer Saline (PBS) for pH 7.3–7.5) were purchased from Fisher Scientific and used without any further purification. For 10 mM PBS solution, the phosphate concentration is about 0.8 mM and the NaCl concentration is about 9.1 mM. The ionic strength of the 10 mM PBS solution is about 11.4 mM. The spherical shape 26 and 60 nm carboxyl functionalized PS NPs were purchased from Bangs Laboratory, Inc. and the spherical shape 10 and 40 nm GNPs were bought from BBI Solutions. The size and shape of the purchased NPs have been verified by scanning electron microscope, dynamic light scattering (DLS) and UV–vis spectroscopy (for GNPs only). Redox molecule Hexaammineruthenium (III) chloride [Ru $(NH_3)_6Cl_3$] (98% pure) was purchased from Sigma-Aldrich. All solutions were prepared using DI water (~18 MΩ) (Ultra Purelab System, ELGA/Siemens).

2.2. Electrochemical measurements

The fabrication and characterisation methods of the nanopore-CNE nanopipette have been reported previously [38]. The ionic current–time (*i–t*) and potential-time (*V–t*) traces are recorded using the experimental setup illustrated in figure 1(a). Axopatch 200B amplifier (Molecular Devices Inc., CA) is used in the voltage clamp mode to measure the current. A home-built high input impedance differential amplifier is used to measure the open-circuit potential V of

the CNE. An oscilloscope (Yokogawa DL850) is used to record the data with a sampling rate of 50 kHz. The bandwidth of the low-pass filter is 5 kHz for current and 40 kHz for potential signals. All the measurements are performed at room temperature. The GNP and PS NP concentrations in the bath solution (10 mM PBS) are typically 10 pM and 100 pM, respectively, if not mentioned otherwise.

2.3. Dielectrophoretic enrichment of NPs

We apply a DC/AC DEP hybrid method to accumulate NPs near the CNE [38]. A dielectric object in a dielectric medium experiences a large DEP force when exposed to a spatially nonuniform electric field. Because of the tip geometry, the DC nanopore bias (V_{pore}) can also generate DC DEP force on the NPs near the nanopipette apex. However, the most effective means is to apply an AC bias on the CNE. A relatively big V_{pore} ($\sim$0.8 V) is applied initially for about 10–30 min, which slowly gathering NPs near the nanopipette tip. In the next step, an AC voltage of 20 V peak-to-peak magnitude and 2 MHz frequency is applied to the CNE for 1–3 min using a function generator (Stanford Research Systems DS340). The CNE is at the centre of a grounded circular ($r = 0.5$ mm) platinum (Pt) wire electrode. The switch in figure 1(a) is used to apply the AC DEP trapping (at position 2). After AC DEP trapping, the switch is changed to position 1 to record signals. As shown in our calculations (see supplementary information S3, available online at stacks.iop.org/NANO/31/015503/mmedia), both PS NP and GNP experience positive DEP forces but the GNP with a higher polarizability is exerted a bigger DEP force.

2.4. Dark-field microscopy (DFM)

The DFM images were captured by a CCD camera (Point Grey Grasshopper 3) on an inverted optical microscope (Nikon Eclipse Ti-U) equipped with a dark-field condenser (Nikon, Ti-DF, NA $\sim$0.8–0.95) and a 40x objective lens (NA = 0.6).

2.5. Data analysis

The data were analysed using custom LabVIEW programmes and OriginPro 2018. The current and potential results are smoothed by a moving average method with 0.1 ms and 0.2 ms time windows, respectively. The dV/dt curves are smoothed by the moving average method using a 3 ms time window if not mentioned otherwise.

3. Results and discussions

3.1. Detecting single-NP collision events

The nanopore-CNE nanopipette used in the experiment has a long-taper geometry with the nanopore diameter in the range of 50–90 nm. The average effective surface area of the CNE is 0.42 μm^2. Systematic measurements have been carried out using 7 nanopipettes (see supplementary table S1) and both insulating PS NPs and conductive GNPs. From the DLS based zeta potential measurements in 10 mM PBS, the zeta potentials of the 26 nm and 60 nm PS NP are found to be -47.4 ± 3.6 mV and -56.3 ± 4.4 mV, respectively. Similarly, -20.2 ± 4.5 mV and -34.2 ± 5.1 mV are the zeta potentials for 10 nm and 40 nm GNP, respectively. The error is the standard deviation of 5 measurements.

The schematic of the experimental setup is shown in figure 1(a). Before adding NPs in the bath solution, both *i–t* and *V–t* time traces are featureless and very stable. After adding NPs, current and potential changes appeared in the traces, indicating that single-NP events happened at the apex. With both nanopore and nanoelectrode at the nanopipette apex, the NPs can interact with the tip in different ways, including translocation through the nanopore, collision at the nanopore orifice sidewall, and collision at the nanoelectrode. However, due to the large electrostatic repulsion forces from the negatively charged long-taper nanopipette tip, the events rate of these events are low under V_{pore}. Especially, the NP-CNE collision event is rarely observed. Following previous reports, [38, 40–42] we employed DEP to boost the event rate (see Experimental section). The AC bias on the CNE effectively concentrates the NPs near the nanopipette tip [42, 43] and triggers continuous translocation or collision events of individual NPs at a high event rate. We found that the AC DEP application time is critical for producing different type of NP events. A short AC DEP trapping time between 30 sec and 1 min often produces translocation events or collision events at the nanopore circumference [38]. By slightly increasing the AC DEP time to 1–3 min, collision events at the CNE dominate. The observed event rate increased at least 30 times after AC DEP and up to a few thousands of collision events can be observed in 20–35 min.

To better understand the accumulation of NPs by the AC DEP forces and the following NP-CNE collision events, we monitored these processes by using the DFM (see methods and supplementary figure S2). The representative DFM videos are shown in supporting information. Without AC DEP, the NPs move slowly in random Brownian motion. Occasionally, a NP speeds up and collides with the apex when it wanders the vicinity of the apex. Upon applying AC DEP, all the NPs in the field of view speed up and move towards the CNE. Similar results have been observed for all the NPs. However, the speeds of the PS NPs under the same AC DEP condition are noticeably slower because of their lower polarizability.

Figure 1(b) shows three sequential DFM snapshots when applying AC DEP forces to trap 40 nm GNPs. The accumulated NPs appear as a bright blob near the nanopipette apex. With the increase of AC DEP trapping time, the size and brightness of the 'blob' increase rapidly, indicating the efficient accumulation of NPs from solution to the nanopipette apex. Although the blob size increased continuously with the AC DEP trapping time, the NP trapping efficiency gradually drops. At the first 30 s of the AC DEP trapping time, the NPs move very fast towards the apex. Thereafter, the speed of NP is greatly reduced and a big fraction of GNPs are scattered away from the tip apex before reaching and joining the 'blob'.

With the increased number of accumulated NPs near the apex, the electrostatic repulsive force is increased and the DEP force is likely reduced due to screening by the accumulated NPs. Interestingly, the baseline of *i–t* trace is unaltered by the NP accumulation. In contrast, the baseline of *V–t* trace descends dramatically (more negative) with the presence of 'blob'. This suggests that the DEP force steers the NPs closer to the CNE side, without affecting the ion flux through the nanopore. This is consistent with the observation that the position of 'blob' is shifted to the CNE side with the increase of AC DEP time (figure 1(b) and supplementary figure S2).

It is worth mentioning that the small size of CNE further enhances the NP trapping efficiency. We have tested CNEs with effective radii ranging from ∼20 to ∼410 nm. Revealed by the DFM, the CNEs with smaller radii, i.e. radius <100 nm, consistently show a higher trapping efficiency than the bigger ones. Because of the small size of CNE, we can effectively trap NPs as small as 10 nm GNPs and 26 nm PS NPs in up to 20 mM PBS solution. In 30 mM PBS solution, we hardly see any directional movement of NPs towards the CNE because the weaker AC DEP force cannot overcome other opposing factors, including electrostatic force, entropy cost, concentration gradient, and electrothermal flow [41].

After AC DEP trapping, the 'blob' gradually reduces in size and brightness but remains distinguishable near the nanopipette tip for more than 30 min The size reduction of blob happens slowly and smoothly, no dramatic changes are observed in the DFM images. Meanwhile, electrochemical signals of individual NP-CNE collision events appear at a high event rate. Therefore, the recorded collision events in *i–t* and *V–t* traces are from the NPs within the blob. The NPs at the inner frontier of the blob are highly dynamic and collide with the CNE continuously.

3.2. Detecting single-NP collision events in a crowded environment

Now we describe the electrochemical recordings of NP collision events at the CNE. We can tell if the signals are from the NP translocation events through the nanopore, the NP collision events at the nanopore circumference during translocation, or the NP-CNE collision events, based on the current changes in the simultaneously recorded *i–t* traces. A typical NP-CNE collision event induces obvious potential changes of CNE but no or very small current changes of nanopore. Comprehensive studies have been carried out by two nanopipettes P2 and P4 (table S1). We compare the potential changes induced by single-NP collision events at the CNE surface in a crowded environment between PS NPs and GNPs. Although translocation events still appear from time to time in the recorded data (supplementary figure S4 (b)), we only discuss the collision events at the CNE surface.

Figure 2(a) shows the event rate (/s) and potential baseline change as a function of time for 60 nm PS NPs in the first 35 min following the AC DEP trapping. Based on Nernst equation, the overall potential baseline change reflects the local NP concentration change near the CNE, which is the collective contribution from all the NPs nearby. At the first 10 min, the potential baseline continues to drop. However, the individual collision event is rarely detected. Therefore, the concentrated NP assembly slowly moves toward the CNE driven by V_{pore}. Between 10 and 30 min, multiple peaks appear in the event rate plot. The arrival of accumulated NPs triggers continuous single-NP collision events. Without pre-accumulating NPs, we rarely observe these events even at a large V_{pore}. Therefore, the increased local NP concentration gradient and the electrostatic repulsion between NPs should be the leading causes for the increased NP-CNE collision events. Indeed, we found that the maxima event rate is mainly determined by the AC DEP trapping time, but not by the V_{pore} after the trapping. The shape of the transient potential change signal is also strongly correlated to the event rate, which also reflects the real-time NP concentration close to the potential sensing zone of CNE. Because of the varying event rate, the effect of V_{pore} to the shape of potential signals is uncertain and inconclusive. This is different from the translocation signals, where both current spikes and potential signals are clearly affected by V_{pore} [38].

Figure 2(b) presents the typical time traces for 60 nm PS NP near the maximum event rate (denoted by a red arrow in figure 2(a)). More data can be found in supplementary figure S4 (a). The baseline of *i–t* trace (the gray colour trace) is stable and featureless, suggesting no translocation events. In contrast, continuous small potential dips appear in the *V–t* trace (the red colour trace). Each potential dip represents a NP-CNE collision event. The potential dip features gradual decrease (more negative) and then a sharp increase in potential. The black colour dash line represents the baseline of the *V–t* trace. The potential baseline is usually stable but can become dramatically more negative and unstable when a big NP cluster moves toward the CNE as shown in the potential baseline plot in figure 2(a). As indicated in the zoom-in trace, there are two types of potential dips, (i) and (ii), based on their shapes. The comparison of the two is illustrated in figure 2(c). In general, the approach time (t_A) is significantly longer (∼5 times) than the rebounding time (t_R) for the type (i) dip. A flattened bottom (green shaded region) appears in type (i) dip, which is named waiting time (t_W). The duration time (t_d) of type (i) dip decreases with the increase of event rate (supplementary figure S4 (a)), mainly due to the decrease of t_W. For type (ii) dip, points 2 and 3 overlap and the t_W fully disappears. Compared with the shape of type (i) dip, the type (ii) dip has a shorter t_d and a smaller potential amplitude (ΔV). Therefore, the types (i) and (ii) dips are from the events with slow and fast approaching motions, respectively. The type (ii) dips appear only when the event rate is high (typically >2 for PS NP) and is rare when the event rate is low. Instead, type (i) dip dominates at low event rates but is still abundant at high event rates.

Figure 2(d) shows the statistical analysis of 1101 potential dips arose between 10 and 25 min. The histograms of t_d and ΔV are shown at the top and right sides of the $t_d - \Delta V$ scatter plot, respectively. Two peaks appear in both histograms, attributing to types (i) and (ii) potential dips. The mean t_d and ΔV of the type (i) potential dip are about 98.8 ± 49.6 ms and 1.14 ± 0.65 mV, respectively. The mean

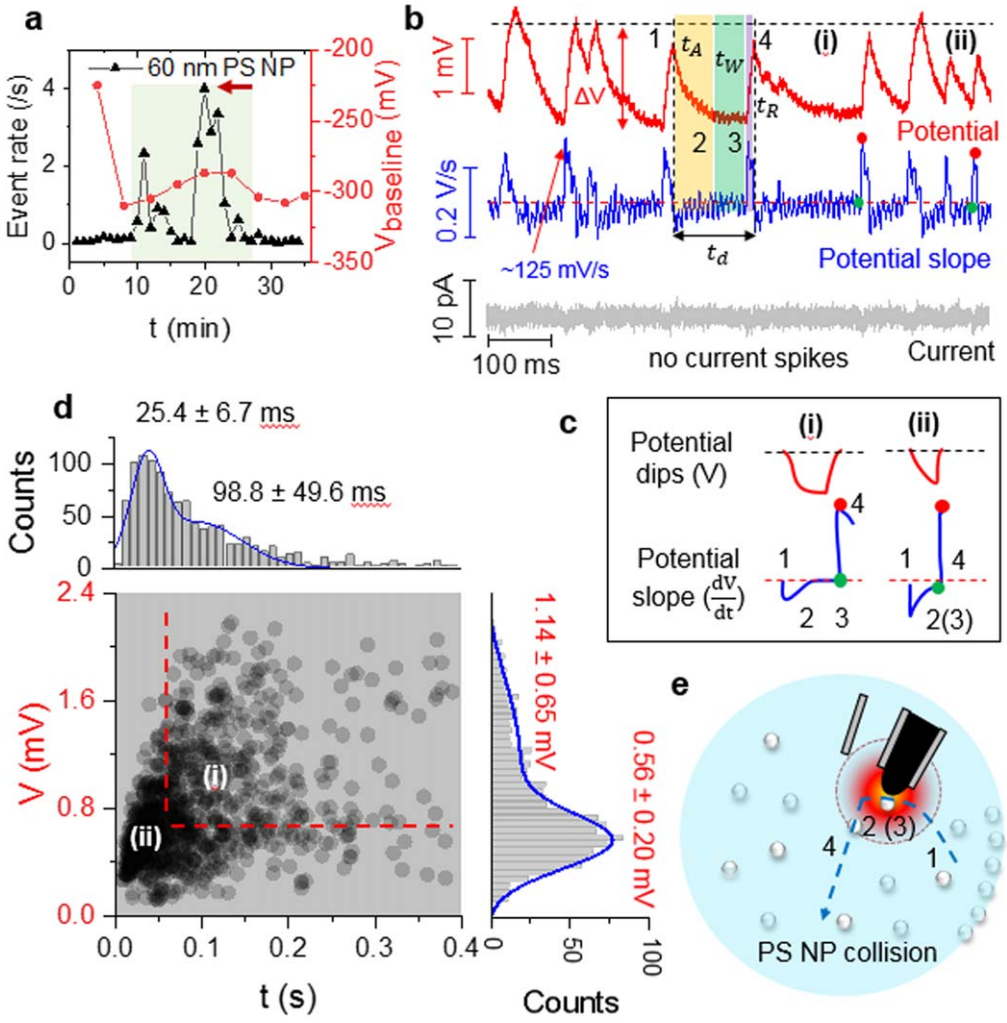

Figure 2. NP-CNE collision events of 60 nm PS NP in a crowded environment. (a) The collision event rate and potential baseline as a function of time based on $N = 1289$ collision events after AC DEP trapping. Each event rate and $V_{baseline}$ points are averaged over 1 min and 4 min data, respectively. (b) Current (gray), Potential (red) and derivative of potential (dV/dt) (blue) time traces at $V_{pore} = 200$ mV and about 20 min (denoted by the red arrow in (a)) after AC DEP trapping. Slow and fast events are labelled as type (i) and (ii), respectively. The t_d is divided into t_A, t_W and t_R. ΔV denotes the amplitude of the potential dip. (c) Schematic of the shapes of potential dips and their derivatives for types (i) and (ii) events. (d) The scatter plot and histograms of t_d and ΔV for $N = 1101$ collision events. Dashed lines in the scatter plot separate types (i) and (ii) events. Solid lines in the histograms are two-peak Gaussian fits. (e) A schematic showing the type (i) event in four steps. The dashed line denotes the motion trajectory of the PS NP. The red region indicates the potential sensing zone of CNE.

t_d and ΔV of the type (ii) potential dip are about 25.4 ± 6.7 ms and 0.56 ± 0.20 mV, respectively. Because the measured ΔVs are much smaller than the measured zeta potential of 60 nm PS NP, the PS NP should be still at some distance away from the CNE surface during collision. Only the double layer of the PS NP overlaps with the double layer of the CNE.

As illustrated in figure 2(e), in a typical type (i) potential dip (also see figures 2(b) and (c)), a 60 nm PS NP enters the potential sensing zone of the CNE at time point 1. As the NP moves closer to the CNE, the potential of CNE decreases gradually to become more negative. The decrease of potential is due to the negative charge carried by the PS NP [39]. Because of charge screening, the detected potential change is exponentially dependent on the distance between the NP and the CNE surface. From points 2 to 3, the potential amplitude remains approximately same which suggests that the NP stops and stays near the closest distance to the CNE. At point 3, the potential quickly jumps back, indicating the PS NP bounces back. At point 4, the potential returns to its baseline and the NP should move out of the CNE sensing zone at this time.

The time trace of the first derivative of potential (dV/dt) (blue colour trace) can qualitatively reveal the NP speed during the collision motion. A higher dV/dt value indicates a larger speed. A negative (positive) dV/dt value indicates the forward (backward) motion to (from) the CNE. A large positive dV/dt value peaks at ~ 125 mV s^{-1} during t_R, suggesting the fast rebounding speed of the PS NP from the CNE. In contrast, the negative dV/dt value is very small (~ -11 mV s^{-1}) during approaching (t_A) and becomes almost zero during t_W. The retardation of the PS NP as it approaches the CNE can be attributed to the hindered diffusion [44] and the increased electrostatic repulsion between the negatively charged NP and CNE surface. It is intriguing for the

appearance of waiting time in the type (i) dip. The NP is likely transiently trapped near the CNE surface under a delicate and dynamic balance between all the forces.

The sudden bouncing back of NP can be triggered by thermal fluctuation or the influence of other NPs. At the high event rate, another potential dip always appears immediately after point 4 in the V–t trace. Therefore, the approach of the second NP should be mainly responsible for the release of the trapped one when the event rate is high. At a low event rate (supplementary figure S4 (a)), we sometimes observed the potential value returns to the baseline at point 4 after a long t_W (more than 1.6 s). In such event, the trapped NP may only escape due to thermal fluctuations.

For comparison, we also investigated the collision events by polarisable GNPs. Supplementary figure S4(c) shows the collision event rate (/s) and potential baseline as a function of time for 40 nm GNPs in the first 35 min following AC DEP trapping. The event rate peak at ~6.5 (events s^{-1}) appears between 10 and 20 min. Compared with the plot in figure 2 (a), the higher peak value of GNPs suggests the density of accumulated GNP assembly is higher at the same DEP trapping condition. This is also supported by the significant drop of the potential baseline at the same time.

Figure 3(a) shows the typical results of 40 nm GNP collision events at the CNE near the highest event rate. Statistical analysis of 1009 GNP potential dips collected between 10 and 20 min is shown in supplementary figure S4(c). Two well-separated data sets appear in the $t_d - \Delta V$ scatter plot. Same as the results of PS NP, we attribute the two data sets to types (i) and (ii) potential dips. The general features of both types are illustrated in the inset of figure 3(b). The type (i) dips (see supplementary figure S4(b)), mainly appear at low event rates (typically <3 for GNP). They are from the GNPs with slow approaching motions. In contrast, the type (ii) dips, as shown in figure 3(a), dominate the signal when the event rate is high (typically >3 for GNP). They are from the GNPs with fast approaching motions. For type (ii) dips, the approaching time t_A is short, with almost no retardation during approaching and no t_W. However, it is interesting to note that obvious retardation appears during the rebounding of GNP, which may be attributed to the stronger repulsion by the denser GNP assembly nearby. It should be noted that the shape characteristics of type (ii) dip remains same at lower V_{pore}, i.e. at zero bias (supplementary figure S5). Therefore, the fast approaching motion of GNP is mainly driven by the high local GNP concentration.

Now we investigate the first derivative of potential dips. In figure 3(a), the dV/dt of the type (ii) dip has a bigger negative peak value (~−95 mV s^{-1} at the green dot) and a smaller positive peak value (~+68 mV s^{-1} at the red dot). Both the positive and negative dV/dt peak values are similar for most of the events. The relatively small positive dV/dt peak also reflects the retardation during GNP rebounding. The negative dV/dt peak is close to a rectangular shape, which reflects the uniform approaching speed. The retardation is very small when GNP approaching the CNE surface, which is very different from the approaching behaviour of the PS NP. The origin of this difference is attributed to the different

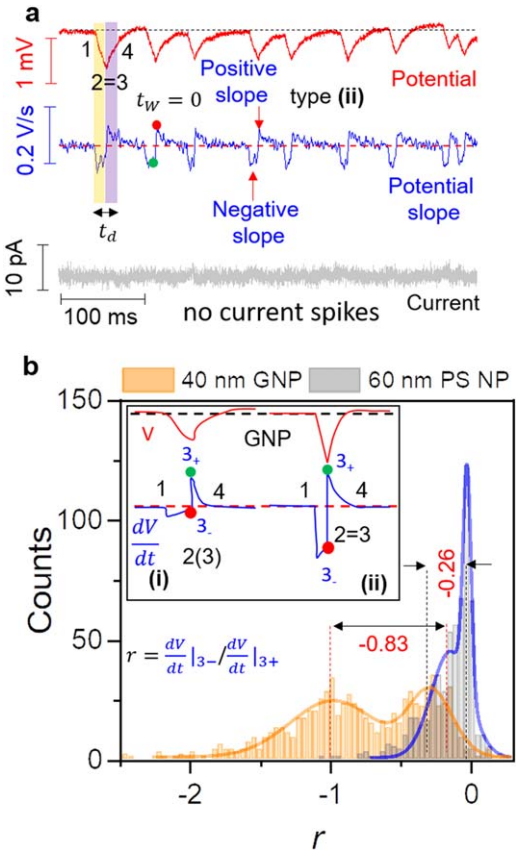

Figure 3. The NP-CNE collision events of 40 nm GNP in a crowded environment. (a) Typical current (gray), potential (red) and the first derivative of potential (blue) time traces. The data are collected when $V_{pore} = 800$ mV is applied. (b) The histograms of r for PS NP ($N = 586$) and GNPs ($N = 788$) with Gaussian fits (solid lines). Inset illustrates of shapes of types (i) and (ii) potential dips of GNP and their derivatives. Parameter r is defined based on dV/dt peaks. Green and red dots denote the dV/dt value just before (i.e. at 3_-) and after (i.e. at 3_+) the point 3.

polarizability, leading to the faster motion of the GNP. When the event rate is low, the approaching speed of GNP is noticeably reduced. As shown in supplementary figure S5(b) and figure 3(b) inset, the negative dV/dt peak of type (i) dip is much smaller and the retardation during approaching is also observed, leading to a triangle type negative dV/dt peak.

As illustrated in figures 2(c) and 3(b) inset, the differences in the collision motions of the PS NP and GNP are clearly reflected in the shapes of potential dips and their time derivatives. These differences can be employed to differentiate NPs. To quantify the differences, we define a dimensionless parameter r. As shown in figure 3(b), r is the ratio between the dV/dt values at the base and peak of the positive dV/dt peak near point 3 (which is the turning point from the approaching motion to rebounding motion), indicated by the green and red dots. In other words, r is the ratio of the potential slopes right before (3_-) and after (3_+) the point 3. A bigger r value reflects the higher approaching speed of the NP and vice-versa. For PS NP, because the approaching motion is slowed down (for type (ii) dip) or fully stopped (for type (i) dip), the $dV/dt|_{3-}$ value is approximately zero. Therefore,

r for PS NP is very small for both type of dips. In contrast, because the retardation is not obvious in GNP approaching motion for both types of dips, the $dV/dt|_{3-}$ is relatively bigger, resulting larger r.

The histograms of r for both 60 nm PS NP and 40 nm GNP collision events are shown in figure 3(b). The mean values of r for 60 nm PS NPs are -0.02 ± 0.03 for the peak and -0.14 ± 0.13 for the shoulder. The almost zero peak value reflects the severe retardation or transiently trapped state of the PS NP near the CNE during approaching. The shoulder is contributed by a fraction of type (ii) fast events with less retardation. Two well-separated peaks appear in the histogram of r for 40 nm GNP. The two peaks are at -0.97 ± 0.31 and -0.28 ± 0.15, from fast type (ii) dips (mainly appear at high event rates) and slow type (i) dips (appear at low event rates), respectively. The difference of r between two types of NPs is much bigger (0.83) for fast events (type (ii)) at high event rates, suggesting we can differentiate the NPs in a crowded environment just based on r.

3.3. Real-time discrimination of GNP and PS NP in a mixture

To further demonstrate the capability of differentiating metallic and insulating NPs in aqueous solutions based on potentiometric measurement of the NP-CNE collisions, a mixture sample of 40 nm GNP and 26 nm PS NP in 1:5 molar concentration ratio (10 pM versus 50 pM) was used. We used a lower GNP concentration in the mixture because of a higher trapping efficiency for the GNPs than for the PS NPs. The nanopipette P1 was used to acquire the results.

The cumulative collision event rate (/s) (produced by both NPs) and potential baseline as a function of time are displayed in figure 4(a). 1 min of AC DEP was first applied to produce 30 min of data. Then 3 min of AC DEP trapping is applied again to generate more collision events in the following ∼35 min The collision event rate becomes significantly higher following the second AC DEP application. Accordingly, the potential baseline drops around 10 min and drops further around 35 min The baseline returns back around 70 min, suggesting the almost full dissipation of the NP accumulations. About 7000 total collision events are observed in the experiment. As we will show later, the PS NP and GNP signals can be distinguished based on the shape of potential dip and the corresponding dV/dt peaks. The GNPs generate about 49% collision signals and the PS NPs generate the rest. This percentage is very different from the initial ∼16.7% of GNPs in the mixture. The significant percentage change confirms the bigger DEP force experienced by the GNPs in the solution.

Multi-peak features are obvious in the event rate plot in figure 4(a). Therefore, the density of accumulated NP mixtures near the nanopipette apex is heterogeneous. Interestingly, the PS NPs and GNPs always separate from each other to form their own clusters (supplementary figure S6). Even at a low event rate (<3 for mixture), the NPs of the same type like to form small clusters. The detected GNP cluster size varied from 2 to ∼9 particles at low event rate and 12 to ∼720 particles at high event rates. In contrast, the cluster size for the PS NPs ranged from 6 to ∼9 at low event rate and 6 to ∼66 at high event rates.

Figure 4(b) shows the data at the low event rate ∼3 events min^{-1} (indicated by light red shaded region in figure 4(a)). Two different types of potential dips are observed in the V–t trace corresponding to PS NP and GNP collision events. Different from the pure NP sample, the events in the mixture appear in small clusters and the shapes of dips in a cluster are similar. Based on the shapes of potential dips and their first derivatives, the signals from 26 nm PS NP are indicated by a light gray bar and from 40 nm GNP are indicated by a light-yellow bar. The t_d of the GNP-CNE collision event is much shorter than the PS NP-CNE collision event. Based on the shapes of these dips, they are type (ii) dips of PS NPs and GNPs. This is surprising, considering that type (ii) dips only appear at high event rates in pure NP samples. The small cluster form likely speed up the motion of individual NPs because of the stronger inter-particle interaction in a cluster. As we discussed for the pure PS NP sample, at a low event rate, the slower PS can be trapped near the CNE. Here, t_W does not show up in the clustered potential dips of PS NPs. The t_W is only obvious in the last collision event of a PS NP cluster and before the arrival of a GNP cluster. This also reflects a smaller inter-particle distance and a bigger inter-cluster distance. Also, both the positive and negative dV/dt peaks are higher. So the motion of individual PS NP in a cluster is much faster even at a low event rate.

We further analysed the ratio r for the potential dips of both NPs at low event rates. The histogram of r is shown in figure 4(c). Two peaks are well-separated. The left peak is from GNP and the right peak is from PS NP. It is apparent from the histogram that more than 95% of the PS NP collision events have an r value more positive than −0.1. $r = -0.1$ can be used as a parameter to separate two types of NPs based on the recorded potential dips. Compared with the histograms in figure 3(b), the mean r value for type (ii) dips of GNPs reduces about 65%, which is attributed to the relatively high rebounding speed. This difference suggests that NP-CNE collision event is strongly affected by the cluster formation in the NP mixture.

Figure 4(d) presents the typical data at a high event rate, as indicated by the light blue shaded region in figure 4(a). The potential baseline fluctuates significantly, which is mainly due to the arrival and departure of large GNP clusters near the CNE. The change induced by PS NP cluster is much smaller and is overshadowed by the neighbouring GNP cluster movement. Considering the slightly bigger surface potential of 26 nm PS NP, the difference stems from the different cluster structures [38]. The GNP cluster is highly compact with a higher volume charge density and thus has a larger impact on the CNE potential. Along with the potential baseline change, the clustered potential dips from GNP and PS NP collision events appeared alternately. Compared with the data at low event rates in figure 4(b), the cluster size here is much bigger.

Three zoom-in time traces are shown at the right panel of figure 4(d). The potential dips of GNPs (trace (i)) appear much denser (∼125 dips s^{-1}) than the dips of PS NP (∼90 dips s^{-1})

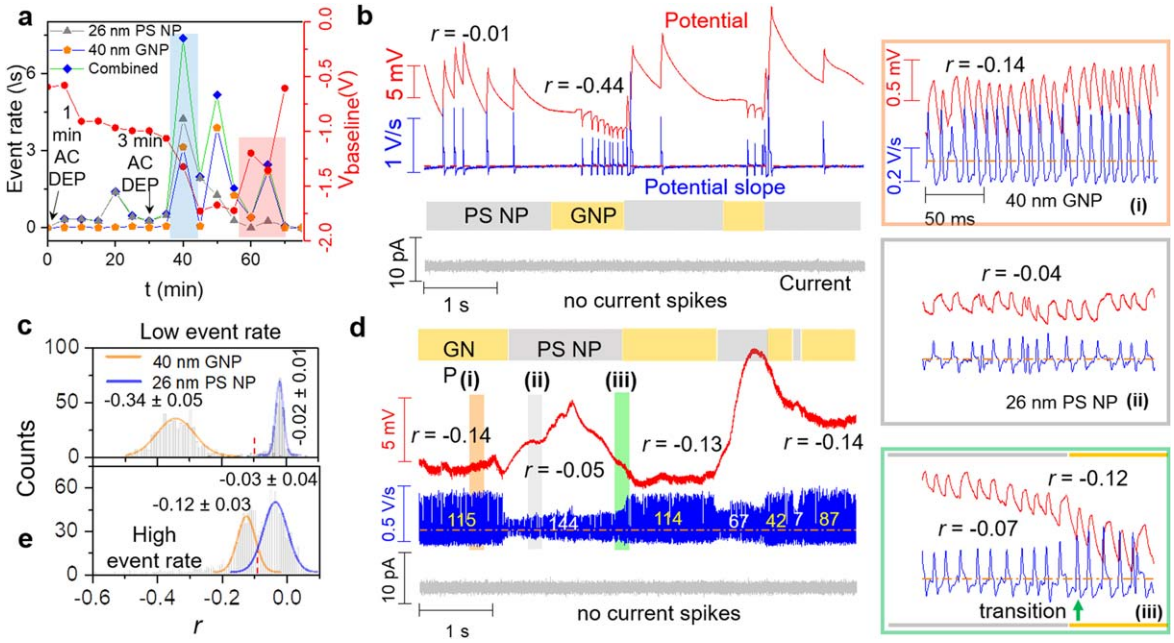

Figure 4. NP-CNE collision events of a mixture of 40 nm GNP and 26 nm PS NP. (a) Single-NP collision event rate and V_{baseline} (red) as a function of time based on $N = 6791$ events in about 75 min after AC DEP trapping. The event rate and V_{baseline} data points are averaged over 5 min The light red and blue shaded regions denote the time window at which collision events shown in (b) and (d) occurred, respectively. (b) I (gray), V (red) and $\mathrm{d}V/\mathrm{d}t$ (blue) time traces at $V_{\text{pore}} = 800$ mV. The $\mathrm{d}V/\mathrm{d}t$ trace is smoothed with a moving average window of 0.4 ms. (c) The histogram of r collected at low event rates for PS NPs ($N = 252$) and GNPs ($N = 523$). (d) NP collision events at high event rates. The numbers on the $\mathrm{d}V/\mathrm{d}t$ time trace denote the number of collision events. At the right panel, the zoom-in of regions (i) and (ii) are of GNPs and PS NPs collisions, respectively. Region (iii) is where the transition from PS NP to GNPs collision occurs. A green arrow denotes the transition point. (e) The histograms of r at the high event rates ($N = 1201$ combined).

(trace (ii)). These dips are also like type (ii) dips of pure GNP samples. The $\mathrm{d}V/\mathrm{d}t$ peaks of GNPs are uniform in shape, reflecting the ordered GNP cluster structure. In contrast, it is less uniform for PS NPs. Both types (i) and (ii) dips appear in the trace. The retardation is obvious in the approaching motion of PS NP collision events. In addition, the potential dips of PS NP are affected by the neighbouring GNP clusters, with varying $\mathrm{d}V/\mathrm{d}t$ peak heights. Here, both positive and negative $\mathrm{d}V/\mathrm{d}t$ peak heights are reduced compared with the peak heights at the low event rate (figure 4(b)). The positive $\mathrm{d}V/\mathrm{d}t$ peak amplitude is reduced more than half. So the rebounding speed of the PS NP after the collision is also greatly hindered by the high local NP density.

Figure 4(e) presents the histogram of r of events at high event rates. The magnitude of r for GNP is further reduced. At high event rates, the approaching speed of GNP decreases more than its rebounding speed, leading to a smaller magnitude of r. In contrast, the magnitude of r for PS NP is slightly increased. As shown in zoom-in trace (iii), the approaching speed of PS NP is slightly faster with less retardation, affected by neighbouring GNPs. The mean value of r for the GNPs and PS NPs collisions are -0.12 ± 0.03 and -0.03 ± 0.04, respectively. Therefore, the separation of r values between the two types of NPs at high even rates is smaller than that at low even rates (figure 4(d)). This is opposite to the change of r in pure NP sample (figure 3(b)). The cluster formation of NP in a mixture obviously altered the collision motion of individual NPs. It is important to note that over 90% of the r value of the PS NPs collision is still more positive than ~ -0.1. Thus, the condition $r = -0.1$ can still be applied to separate GNPs from PS NPs.

Finally, we should mention that the proximity of the nanopore next to the CNE demonstrates several advantages although the nanopore is not directly used as the detector in the NP-CNE collision events. (i) Right after AC trapping, the DC bias applied at the nanopore barrel helps drive the accumulated NPs closer to the nanoelectrode to trigger the continuous potentiometric detection of collision events by individual NPs at the CNE. The V_{pore} also helps retain the accumulated NPs and prevents them moving in random directions during measurements. (ii) Surprisingly, few NP adsorption events are detected in these events. The contamination-free CNE surface is critical for long-time measurements. We speculate that the focused electric field and electroosmotic flow in/out of the nanopore likely prevent the NP staying at the CNE surface. (iii) The simultaneously recorded ionic current signal still provides important information regarding the type of NP events at the nanopipette apex.

4. Conclusions

In summary, we reported the effective generation and detection of single-NP collision events at the nanoelectrode in solutions using a nanopore–nanoelectrode nanopipette. By applying the AC DEP force through the CNE at the nanopipette apex, we can accumulate a large number of NPs near

the CNE in a few minutes and produce NP-CNE collision events with a high event rate for tens of minutes. Between GNPs and PS NPs, the AC DEP trapping is most effective for GNPs. Based on potentiometric measurements using the CNE, we reveal the key differences in the approaching motion between metallic and insulating NPs. The approaching motion of PS NP toward the CNE is obviously slowed down or fully stopped near the CNE, resulting in a distinct change in transient potential change and its first derivative. The individual NP-CNE collision events induced potential changes can also be employed to differentiate the NPs in a mixture. Due to different polarizability, the PS NPs and GNPs separate from each other and form clusters in the concentrated NP mixture. Structural information of these dynamic NP assembly structures can be probed. By integrating the nanopore and nanoelectrode based single-entity electrochemical methods, we expect that the multifunctional nanopipettes have practical applications in biomedical, energy, and environmental studies.

Acknowledgments

This work was supported by the Engineering Research Centre Programme of the National Science Foundation under NSF Cooperative Agreement No. EEC-1647837, NSF CBET 1454544 and NSFC (21673023). The authors would like to thank AMERI at FIU for SEM usage. We also would like to thank Professor Shuai Chang for help with the data analysis software.

ORCID iDs

Popular Pandey https://orcid.org/0000-0002-1899-3480
Jin He https://orcid.org/0000-0002-2633-9809

References

[1] Wang W and Tao N 2014 *Anal. Chem.* **86** 2–14
[2] Kleijn S E F, Lai S C S, Koper M T M and Unwin P R 2014 *Angew. Chem., Int. Ed.* **53** 3558–86
[3] Dykman L and Khlebtsov N 2012 *Chem. Soc. Rev.* **41** 2256–82
[4] Wang Y, Shan X and Tao N 2016 *Faraday Discuss.* **193** 9–39
[5] Baker L A 2018 *J. Am. Chem. Soc.* **140** 15549–59
[6] Howorka S and Siwy Z 2009 *Chem. Soc. Rev.* **38** 2360–84
[7] Kasianowicz J J, Brandin E, Branton D and Deamer D W 1996 *Proc. Natl Acad. Sci. USA* **93** 13770
[8] Shi W, Friedman A K and Baker L A 2017 *Anal. Chem.* **89** 157–88
[9] Harrer S, Kim S C, Schieber C, Kannam S, Gunn N, Moore S, Scott D, Bathgate R, Skafidas S and Wagner J M 2015 *Nanotechnology* **26** 182502
[10] Lin X, Ivanov A P and Edel J B 2017 *Chem. Sci.* **8** 3905–12
[11] Steinbock L J, Otto O, Chimerel C, Gornall J and Keyser U F 2010 *Nano Lett.* **10** 2493–7
[12] Tiwari P B, Astudillo L, Miksovska J, Wang X, Li W, Darici Y and He J 2014 *Nanoscale* **6** 10255–63
[13] Zhou K, Li L, Tan Z, Zlotnick A and Jacobson S C 2011 *J. Am. Chem. Soc.* **133** 1618–21
[14] Sze J Y Y, Kumar S, Ivanov A P, Oh S-H and Edel J B 2015 *Analyst* **140** 4828–34
[15] Yusko E C *et al* 2016 *Nat. Nanotechnol.* **12** 360
[16] Qiu Y, Vlassiouk I, Hinkle P, Toimil-Molares M E, Levine A J and Siwy Z S 2016 *ACS Nano* **10** 3509–17
[17] Terejánszky P, Makra I, Fürjes P and Gyurcsányi R E 2014 *Anal. Chem.* **86** 4688–97
[18] Quinn B M, van't Hof P G and Lemay S G 2004 *J. Am. Chem. Soc.* **126** 8360–1
[19] Xiao X and Bard A J 2007 *J. Am. Chem. Soc.* **129** 9610–2
[20] Peng Y-Y, Qian R-C, Hafez M E and Long Y-T 2017 *Chem. Electro. Chem.* **4** 977–85
[21] McKelvey K, German S R, Zhang Y, White H S and Edwards M A 2017 *Curr. Opin. Electrochem.* **6** 4–9
[22] Couto R A S, Chen L, Kuss S and Compton R G 2018 *Analyst* **143** 4840–3
[23] Oja S M, Wood M and Zhang B 2013 *Anal. Chem.* **85** 473–86
[24] Pumera M 2014 *ACS Nano* **8** 7555–8
[25] Rees N V 2014 *Electrochem. Commun.* **43** 83–6
[26] Anderson T J and Zhang B 2016 *Acc. Chem. Res.* **49** 2625–31
[27] McKelvey K, Robinson D A, Vitti N J, Edwards M A and White H S 2018 *Faraday Discuss.* **210** 189–200
[28] Ma W, Ma H, Yang Z-Y and Long Y-T 2018 *J. Phys. Chem. Lett.* **9** 1429–33
[29] Chen C-H, Ravenhill E R, Momotenko D, Kim Y-R, Lai S C S and Unwin P R 2015 *Langmuir* **31** 11932–42
[30] Stuart E J E, Tschulik K, Batchelor-McAuley C and Compton R G 2014 *ACS Nano* **8** 7648–54
[31] Dasari R, Tai K, Robinson D A and Stevenson K J 2014 *ACS Nano* **8** 4539–46
[32] Zhou Y-G, Stuart E J E, Pillay J, Vilakazi S, Tshikhudo R, Rees N V and Compton R G 2012 *Chem. Phys. Lett.* **551** 68–71
[33] McKelvey K, Edwards M A and White H S 2016 *J. Phys. Chem. Lett.* **7** 3920–4
[34] Kang M, Perry D, Kim Y-R, Colburn A W, Lazenby R A and Unwin P R 2015 *J. Am. Chem. Soc.* **137** 10902–5
[35] Zhou M, Yu Y, Hu K, Xin H L and Mirkin M V 2017 *Anal. Chem.* **89** 2880–5
[36] Kleijn S E F, Lai S C S, Miller T S, Yanson A I, Koper M T M and Unwin P R 2012 *J. Am. Chem. Soc.* **134** 18558–61
[37] Zhou H, Park J H, Fan F-R F and Bard A J 2012 *J. Am. Chem. Soc.* **134** 13212–5
[38] Pandey P, Panday N, Chang S, Pang P, Garcia J, Wang X, Fu Q and He J 2018 *Chem. Electro. Chem.* **5** 3102–12
[39] Panday N, Qian G, Wang X, Chang S, Pandey P and He J 2016 *ACS Nano* **10** 11237–48
[40] Tanaka S, Tsutsui M, Theodore H, Yuhui H, Arima A, Tsuji T, Doi K, Kawano S, Taniguchi M and Kawai T 2016 *Sci. Rep.* **6** 31670
[41] Freedman K J, Otto L M, Ivanov A P, Barik A, Oh S-H and Edel J B 2016 *Nat. Commun.* **7** 10217
[42] Freedman K J, Crick C R, Albella P, Barik A, Ivanov A P, Maier S A, Oh S-H and Edel J B 2016 *ACS Photonics* **3** 1036–44
[43] Chen D, Du H and Tay C 2010 *Nanoscale Res. Lett.* **5** 55–60
[44] Eloul S and Compton R G 2016 *J. Phys. Chem. Lett.* **7** 4317–21